J. Fluid Mech. (2015), *vol.* 784, *pp.* 109–129. © Cambridge University Press 2015
doi:10.1017/jfm.2015.597

Transport equation for the isotropic turbulent energy dissipation rate in the far-wake of a circular cylinder

S. L. Tang[1,2], **R. A. Antonia**[2,†], **L. Djenidi**[2] **and Y. Zhou**[1]

[1]Institute for Turbulence-Noise-Vibration Interaction and Control, Shenzhen Graduate School,
Harbin Institute of Technology, Shenzhen 518055, PR China

[2]School of Engineering, University of Newcastle, NSW 2308, Australia

(Received 8 June 2015; revised 7 October 2015; accepted 10 October 2015;
first published online 30 October 2015)

The transport equation for the isotropic turbulent energy dissipation rate $\overline{\epsilon}_{iso}$ along the centreline in the far-wake of a circular cylinder is derived by applying the limit at small separations to the two-point energy budget equation. It is found that the imbalance between the production and the destruction of $\overline{\epsilon}_{iso}$, respectively due to vortex stretching and viscosity, is governed by both the streamwise advection and the lateral turbulent diffusion (the former contributes more to the budget than the latter). This imbalance differs intrinsically from that in other flows, e.g. grid turbulence and the flow along the centreline of a fully developed channel, where either the streamwise advection or the lateral turbulent diffusion of $\overline{\epsilon}_{iso}$ governs the imbalance. More importantly, the different types of imbalance represent different constraints on the relation between the skewness of the longitudinal velocity derivative S and the destruction coefficient of enstrophy G. This results in a non-universal approach of S towards a constant value as the Taylor microscale Reynolds number R_λ increases. For the present flow, the magnitude of S decreases initially ($R_\lambda \leqslant 40$) before increasing ($R_\lambda > 40$) towards this constant value. The constancy of S at large R_λ violates the modified similarity hypothesis introduced by Kolmogorov (*J. Fluid Mech.*, vol. 13, 1962, pp. 82–85) but is consistent with the original similarity hypotheses (Kolmogorov, *Dokl. Akad. Nauk SSSR*, vol. 30, 1941*b*, pp. 299–303 (see also 1991 *Proc. R. Soc. Lond.* A, vol. 434, pp. 9–13)) (K41), and, more importantly, with the almost completely self-preserving nature of the plane far-wake.

Key words: turbulence theory, turbulent flows, wakes

1. Introduction

Kolmogorov's transport equation for the second-order moment of the longitudinal velocity increment Δu_1 (Kolmogorov 1941*a*), derived from the Navier–Stokes equation, is given by (using homogeneity and isotropy)

$$-\overline{(\Delta u_1)^3} + 6\nu \frac{\partial}{\partial r}\overline{(\Delta u_1)^2} = \frac{4}{5}\overline{\epsilon}_{iso} r, \tag{1.1}$$

---

† Email address for correspondence: robert.antonia@newcastle.edu.au

with $\Delta u_1(r) = u_1(x+r) - u_1(r)$, where u_i $(i = 1, 2, 3)$ are the velocity fluctuations in the x, y and z directions, respectively. In this paper, u_1, u_2 and u_3 will be used interchangeably with u, v and w; similarly for x_1, x_2 and x_3 and x, y, z. The first term in (1.1) is the third-order structure function, while the second term represents the viscous effect. The term on the right-hand side of (1.1) is proportional to the isotropic mean energy dissipation rate $\overline{\epsilon}_{iso}$ $(= 15\nu\overline{(\partial u_1/\partial x_1)^2}$, ν is the fluid kinematic viscosity) and balances the sum of the other terms. This equation is of fundamental importance since it is an equilibrium equation between second- and third-order moments and represents a mean turbulent energy balance for each scale, r, when the Reynolds number is sufficiently large and r is small compared with the integral length scale. In small to moderate Reynolds number flows, this equation is usually not satisfied except perhaps at small r since (1.1) does not contain any large-scale term. Additional terms $I_q(r)$ reflecting the influence of the large scales, which may differ from flow to flow, need to be added to (1.1). For example, for decaying homogeneous and isotropic turbulence (HIT), (1.1) becomes (e.g. Danaila *et al.* 1999; Antonia *et al.* 2000; Danaila, Antonia & Burattini 2004; Antonia & Burattini 2006)

$$-\frac{3}{r^4}\int_0^r s^4\left[U\frac{\partial\overline{(\Delta u_1)^2}}{\partial x}\right]\mathrm{d}s-\overline{(\Delta u_1)^3}+6\nu\frac{\partial}{\partial r}\overline{(\Delta u_1)^2}=\frac{4}{5}\overline{\epsilon}_{iso}r, \tag{1.2}$$

where $-(3/r^4)\int_0^r s^4[U(\partial\overline{(\Delta u_1)^2}/\partial x)]\,\mathrm{d}s$ $(\equiv I_q)$ represents a (large scale) streamwise advection term. In (1.2), s is a dummy variable, identifiable with the separation along x; and U is the (constant) mean velocity in the x direction.

More importantly, in the limit $r \to 0$, and selecting terms of order r^3, (1.2) reduces to the transport equation for $\overline{\epsilon}_{iso}$, *viz.*

$$-U\frac{\mathrm{d}\overline{\epsilon}_{iso}}{\mathrm{d}x}=\frac{7}{3\sqrt{15}}\frac{\overline{\epsilon}_{iso}^{\,3/2}}{\nu^{1/2}}\left[S+2\frac{G}{R_\lambda}\right] \tag{1.3}$$

in decaying grid turbulence. This equation was first written and tested by Batchelor & Townsend (1947) and recently analysed in detail by Djenidi & Antonia (2014) using direct numerical simulations.

In (1.3), S (<0) is the skewness of $\partial u_1/\partial x_1$

$$S=\frac{\overline{(\partial u_1/\partial x_1)^3}}{\overline{(\partial u_1/\partial x_1)^2}^{3/2}}, \tag{1.4}$$

G is the non-dimensional enstrophy destruction coefficient of $\overline{\epsilon}_{iso}$

$$G=\overline{u_1^2}\,\frac{\overline{(\partial^2 u_1/\partial x_1^2)^2}}{\overline{(\partial u_1/\partial x_1)^2}^{2}}, \tag{1.5}$$

and R_λ is the Taylor microscale Reynolds number

$$R_\lambda=\frac{\overline{u^2}^{1/2}\lambda}{\nu}, \tag{1.6}$$

where the Taylor microscale λ is defined as the ratio $\overline{u^2}^{1/2}/\overline{(\partial u/\partial x)^2}^{1/2}$. If a power-law decay rate for $\overline{u^2}$ is assumed for grid turbulence, *viz.* $\overline{u^2}\sim x^{-n}$, then (1.3) can be rewritten as (e.g. Thiesset, Antonia & Danaila 2013)

$$\frac{90}{7(1+2R)}\left(\frac{n+1}{n}\right)\frac{1}{R_\lambda}=\frac{C}{R_\lambda}=S+2\frac{G}{R_\lambda}, \tag{1.7}$$

with $C=(90/(7(1+2R)))((n+1)/n)$ and $R=\overline{v^2}/\overline{u^2}$.

Along the axis in the far field of an axisymmetric jet flow where the flow satisfies self-preservation, $I_q(r)$ is given by (Burattini, Antonia & Danaila 2005; Thiesset *et al.* 2013)

$$I_q(r)=-\frac{3}{r^4}\int_0^r s^4\left[U\frac{\partial\overline{(\Delta u_1)^2}}{\partial x}+2\left(\overline{(\Delta u_1)^2}-\overline{(\Delta u_2)^2}\right)\frac{\partial U}{\partial x}\right]\mathrm{d}s, \tag{1.8}$$

where the mean velocity $U\sim x^{-1}$. At small r, (1.8) reduces to (Thiesset *et al.* 2013)

$$I_q=-U\frac{\partial\bar{\epsilon}_{iso}}{\partial x}+2\bar{\epsilon}_{iso}\frac{\partial U}{\partial x}. \tag{1.9}$$

Thus the transport equation for $\bar{\epsilon}_{iso}$ can be written as

$$-U\frac{\partial\bar{\epsilon}_{iso}}{\partial x}+2\bar{\epsilon}_{iso}\frac{\partial U}{\partial x}=\frac{7}{3\sqrt{15}}\frac{\bar{\epsilon}_{iso}{}^{3/2}}{\nu^{1/2}}\left[S+2\frac{G}{R_\lambda}\right], \tag{1.10}$$

which can be rewritten in the form

$$\frac{90}{7(2+R)}\frac{1}{R_\lambda}=\frac{C}{R_\lambda}=S+2\frac{G}{R_\lambda}, \tag{1.11}$$

with $C=90/(7(2+R))$.

For stationary forced periodic box turbulence (SFPBT), the forcing is usually concentrated at very low wavenumbers (i.e. very large scales). For example, the large scale forcing term as used by Fukayama *et al.* (2000) is

$$I_q(r)=\tfrac{2}{35}\epsilon_{in}(k_e r)^2 r, \tag{1.12}$$

where ϵ_{in} is the energy input rate due to external random forces concentrated at a wavenumber $k\simeq k_e$.

One expects that for SFPBT, where the forcing is usually concentrated at very low wavenumbers, the magnitude of C should be much smaller than for decaying turbulence or flows where forcing is spread over a range of wavenumbers. For example, the estimated ratio of the large scale forcing term to S for the SFPBT of Fukayama *et al.* (2000) is approximately 0.016 at $R_\lambda=70$ (estimated from their figure 5) at small separations, while it is several orders of magnitude at $R_\lambda=460$ for the SFPBT of Gotoh, Fukayama & Nakano (2002). In this case, $C\simeq 0$, so that

$$\frac{C}{R_\lambda}=S+2\frac{G}{R_\lambda}\simeq 0. \tag{1.13}$$

Equations (1.7), (1.11) and (1.13) represent, in essence, a constraint on how S varies with R_λ in different flows. Since the ratio G/R_λ approaches a constant relatively rapidly with increasing R_λ (evidence for this was collected by Lee *et al.* (2013)), and the terms on the left-hand sides of (1.7), (1.11) and (1.13) must eventually vanish, the latter three equations imply that the magnitude of S should become constant at sufficiently large R_λ; for SFPBT, S may become constant at a relatively small R_λ. Such an expectation follows almost naturally from Antonia & Burattini (2006) who examined how the 4/5 law (Kolmogorov 1941*a*) is approached with and without forcing.

This is consistent with $K41$ and the predictions of Qian (1994), but in contradiction with the modified similarity hypothesis of Kolmogorov (1962) or $K62$. This latter hypothesis has spawned tremendous interest in how the normalised high-order moments of $\partial u_1/\partial x_1$ vary with R_λ (e.g. Van Atta & Antonia 1980; Sreenivasan & Antonia 1997; Davidson 2004; Wyngaard 2010).

The present paper aims to provide some insight into the transport equation for $\overline{\epsilon}_{iso}$ along the axis in the far wake of a circular cylinder where self-preservation is satisfied to a close approximation. The far-wake has received significant attention both with respect to the type and degree of organisation of the large scale motion, but also with the characteristics of the small scale motion (e.g. Antonia & Browne 1986; Antonia *et al.* 1987; Browne, Antonia & Shah 1987; Antonia, Browne & Shah 1988; Bisset, Antonia & Britz 1990*a*; Bisset, Antonia & Browne 1990*b*; Brown & Roshko 2012). According to Danaila *et al.* (2001), the large scale forcing term $I_q(r)$ on the axis of a plane far-wake is given by

$$I_q(r) = -\frac{3}{r^4}\int_0^r s^4\left[U\frac{\partial\overline{(\Delta u_1)^2}}{\partial x}\right]\mathrm{d}s + \frac{6}{r^4}\int_0^r s^4\left[-\frac{\partial\overline{u_2(\Delta u_1)^2}}{\partial y}\right]\mathrm{d}s. \tag{1.14}$$

The first and second terms on the right-hand side of (1.14) are the large scale forcing terms which arise from the turbulent transport of $\overline{(\Delta u_1)^2}$ by the mean velocity U and the lateral velocity fluctuation u_2. This is different to grid turbulence (1.2), the axisymmetric jet flow along the axis (1.8) and SFPBT (1.12), thus implying that the physics associated with the transport of $\overline{\epsilon}_{iso}$ may differ in each flow. One then expects that the manner in which S approaches a constant as R_λ increases may differ from flow to flow. By considering the limit at small separations of the two-point energy budget equation, a transport equation for $\overline{\epsilon}_{iso}$ can be obtained. The dependence of S on R_λ which ensues from this equation can then be compared with measured values of S.

This paper is structured as follows. In § 2, we derive the transport equation for $\overline{\epsilon}_{iso}$ which yields a relation between S, G and R_λ (shown in § 3). Details associated with the measurements are described in § 4. Experimental support for this relation is discussed in § 5. The implication, based on this relation, for the dependence of S on R_λ when the ratio G/R_λ is approximately constant is also given in § 5. We also discuss this implication in the context of the modified similarity hypothesis of $K62$. The way in which $S+2G/R_\lambda$ approaches zero as R_λ increases is compared with that in other flows, namely decaying grid turbulence, along the axis in the far field of an axisymmetric jet and SFPBT. Conclusions are given in § 6.

2. Transport equation for $\overline{\epsilon}_{iso}$ on the centreline of the far-wake

According to Danaila *et al.* (2001), the isotropic form of the scale-by-scale energy budget equation on the axis of a plane far-wake is given by

$$\begin{aligned}-\frac{3}{r^4}\int_0^r s^4\left[U\frac{\partial\overline{(\Delta u_1)^2}}{\partial x}\right]\mathrm{d}s + \frac{6}{r^4}\int_0^r s^4\left[-\frac{\partial\overline{u_2(\Delta u_1)^2}}{\partial y}\right]\mathrm{d}s - \overline{(\Delta u_1)^3}\\ +6\nu\frac{\partial}{\partial r}\overline{(\Delta u_1)^2} = \frac{4}{5}\overline{\epsilon}_{iso}r.\end{aligned} \tag{2.1}$$

Using a Taylor series expansion about $r=0$, $\overline{(\Delta u_1)^2}$ can be approximated by

$$\overline{(\Delta u_1)^2} \approx \overline{\left(\frac{\partial u_1}{\partial x}\right)^2} r^2 - \frac{1}{12}\overline{\left(\frac{\partial^2 u_1}{\partial x^2}\right)^2} r^4 + O(r^6), \tag{2.2}$$

while

$$\lim_{r\to 0} \frac{3}{r^4}\int_0^r s^4 \left[U\frac{\partial \overline{(\Delta u_1)^2}}{\partial x}\right] \mathrm{d}s = \frac{1}{35} U \frac{\mathrm{d}\overline{\epsilon}_{iso}}{\mathrm{d}x} r^3, \tag{2.3}$$

and

$$\begin{aligned} \lim_{r\to 0} \frac{6}{r^4}\int_0^r s^4 \left[\frac{\partial \overline{u_2(\Delta u_1)^2}}{\partial y}\right] \mathrm{d}s &= \lim_{r\to 0} \frac{6}{r^4}\int_0^r s^4 \left[\frac{\partial \overline{u_2\left(\dfrac{\partial u_1}{\partial x}\right)^2 r^2}}{\partial y}\right] \mathrm{d}s \\ &= \frac{6}{7}\frac{\partial \overline{\left[u_2\left(\dfrac{\partial u_1}{\partial x}\right)^2\right]}}{\partial y} r^3. \end{aligned} \tag{2.4}$$

We recall that the instantaneous energy dissipation rate ϵ is given by (e.g. Hinze 1975)

$$\begin{aligned} \epsilon &= \nu\left(\frac{\partial u_i}{\partial x_j}+\frac{\partial u_j}{\partial x_i}\right)\frac{\partial u_j}{\partial x_i} \\ &= \nu\left\{2\left(\frac{\partial u_1}{\partial x_1}\right)^2+\left(\frac{\partial u_2}{\partial x_1}\right)^2+\left(\frac{\partial u_3}{\partial x_1}\right)^2+\left(\frac{\partial u_1}{\partial x_2}\right)^2\right. \\ &\quad +2\left(\frac{\partial u_2}{\partial x_2}\right)^2+\left(\frac{\partial u_3}{\partial x_2}\right)^2+\left(\frac{\partial u_1}{\partial x_3}\right)^2+\left(\frac{\partial u_2}{\partial x_3}\right)^2+2\left(\frac{\partial u_3}{\partial x_3}\right)^2 \\ &\quad \left.+2\left(\frac{\partial u_1}{\partial x_2}\right)\left(\frac{\partial u_2}{\partial x_1}\right)+2\left(\frac{\partial u_1}{\partial x_3}\right)\left(\frac{\partial u_3}{\partial x_1}\right)+2\left(\frac{\partial u_2}{\partial x_3}\right)\left(\frac{\partial u_3}{\partial x_2}\right)\right\}. \end{aligned} \tag{2.5}$$

Equation (2.4) can be rewritten as follows

$$\frac{6}{7}\frac{\partial \overline{\left[u_2\left(\dfrac{\partial u_1}{\partial x_1}\right)^2\right]}}{\partial x_2} r^3 = \frac{3}{7\nu}\frac{\partial \overline{\left[2\nu u_2\left(\dfrac{\partial u_1}{\partial x_1}\right)^2\right]}}{\partial x_2} r^3 = \frac{3}{7\nu}\frac{\partial \overline{u_2\epsilon_1}}{\partial x_2} r^3, \tag{2.6}$$

where $\epsilon_1 = 2\nu(\partial u_1/\partial x_1)^2$ is only one component of the instantaneous energy dissipation rate ϵ.

After substituting (2.3), (2.2), (2.4) and (2.6) in (2.1), replacing $\lim_{r\to 0}\overline{(\Delta u_1)^3}$ by $\overline{(\partial u_1/\partial x_1)^3} r^3$ and equating terms in r^3, we obtain

$$-\frac{1}{35\nu} U \frac{\partial \overline{\epsilon}_{iso}}{\partial x} - \frac{3}{7\nu}\frac{\partial \overline{u_2\epsilon_1}}{\partial y} = \overline{\left(\frac{\partial u_1}{\partial x}\right)^3} + 2\nu\overline{\left(\frac{\partial^2 u_1}{\partial x^2}\right)^2}, \tag{2.7}$$

which can be recast in the form

$$\underbrace{-\frac{1}{35\nu}U\frac{\partial\bar{\epsilon}_{iso}}{\partial x}\Big/\left[\frac{\bar{\epsilon}_{iso}^{3/2}}{(15\nu)^{3/2}}\right]}_{Advection}\underbrace{-\frac{3}{7\nu}\frac{\partial\overline{u_2\epsilon_1}}{\partial y}\Big/\left[\frac{\bar{\epsilon}_{iso}^{3/2}}{(15\nu)^{3/2}}\right]}_{Diffusion}=S+2\frac{G}{R_\lambda}. \tag{2.8}$$

Equation (2.8) is the transport equation for $\bar{\epsilon}_{iso}$ on the centreline of a far-wake. Note that it differs from the transport equation of $\bar{\epsilon}_{iso}$ in grid turbulence since, in addition to the streamwise advection term for $\bar{\epsilon}_{iso}$ on the left-hand side of (2.8), a cross-flow transport term for $\bar{\epsilon}_{iso}$ also contributes to the imbalance between S and $2G/R_\lambda$.

3. A relation for S, G and R_λ on the centreline of the far-wake

Following the same procedure as Thiesset, Antonia & Djenidi (2014), Tang *et al.* (2015*b*) applied a self-preservation analysis to the scale-by-scale energy budget equation and showed that in the far-wake of a cylinder the evolution of $\bar{\epsilon}_{iso}$ can be written as

$$\frac{\bar{\epsilon}_{iso}d}{U_\infty^3}=A_u^2R_\epsilon(1+2R)\left(\frac{x}{d}-\frac{x_0}{d}\right)^{-2}, \tag{3.1}$$

where x_0 is the effective flow origin; $R=\overline{u_2^2}/\overline{u_1^2}$ which represents a measure of large scale anisotropy; the approximation $u_2^2=u_3^2$, supported by the measurements on the centreline of the far wake (Hao *et al.* 2008), was used; A_u is the power-law prefactor for $\overline{u^2}^{1/2}$, i.e.

$$\frac{\overline{u^2}}{U_\infty^2}=A_u^2\left(\frac{x-x_0}{d}\right)^{-1}; \tag{3.2}$$

and R_ϵ is the ratio of the isotropic mean energy dissipation rate to the full mean energy dissipation rate, *viz.* $R_\epsilon=\bar{\epsilon}_{iso}/\bar{\epsilon}$. Tang *et al.* (2015*b*) also showed that the relation between R_d and R_λ is given by

$$\frac{R_\lambda}{R_d^{1/2}}=\left[\frac{15A_u^2}{(1+2R)R_\epsilon}\right]^{1/2}. \tag{3.3}$$

Equations (3.1) and (3.3) have been tested by Tang *et al.* (2015*b*) and found to be well supported by measurements in the far-wake. With regard to the advection term in (2.8), we obtain, after substituting (3.1) and (3.3) into the advection term on the left-hand side of equation (2.8)

$$-\frac{1}{35\nu}U\frac{\partial\bar{\epsilon}_{iso}}{\partial x}\Big/\left[\frac{\bar{\epsilon}_{iso}^{3/2}}{(15\nu)^{3/2}}\right]=\frac{90}{7(1+2R)R_\epsilon R_\lambda}=\frac{C_a}{R_\lambda}, \tag{3.4}$$

where C_a is given by

$$C_a=\frac{90}{7(1+2R)R_\epsilon}. \tag{3.5}$$

With regard to the diffusion term, figure 1 shows the distribution of $-(3/7\nu)\overline{u_2\epsilon_1}$, as a function of y/L_0, obtained with a one-component vorticity probe (a detailed description of the probe and measurements is given in Lefeuvre *et al.* (2014); R_d is 1400 and the corresponding R_λ is approximately 40 on the centreline), where three

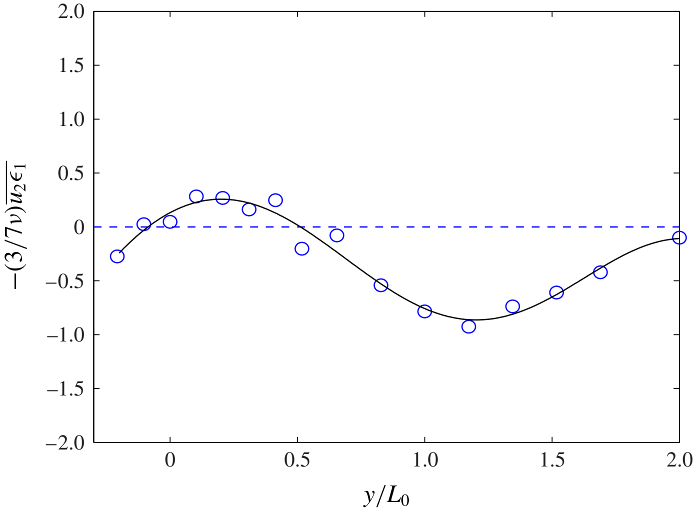

FIGURE 1. (Colour online) Distribution of $-(3/7\nu)\overline{u_2\epsilon_1}$ with y/L_0 at $x/d = 240$ and $R_d = 1400$ ($R_\lambda = 40$ on the flow centreline). The solid curve is a seventh-order polynomial fit. The horizontal dashed line corresponds to $\overline{u_2\epsilon_1} = 0$.

different measurements of u_1 are made simultaneously with u_2 at each y location. Each point shown in figure 1 is an average of three values, as obtained from three different hot wires. Interestingly, the distribution of $-(3/7\nu)\overline{u_2\epsilon_1}$ is similar to that of $\overline{u_2u_i^2}$ (Browne *et al.* 1987; Lefeuvre *et al.* 2014) suggesting that the diffusion of $\overline{q^2}$ (i.e. large scales) by u_2 has the same characteristics as the diffusion of ϵ_1 (i.e. small scales) by u_2. The diffusion term on the left-hand side of (2.8) is obtained by applying a seventh-order polynomial fit to the distribution of $-(3/7\nu)\overline{u_2\epsilon_1}$ over the range $y/L_0 = -0.2$–2, and then normalising the slope of the fitted curve at $y/L_0 = 0$ with $\bar{\epsilon}_{iso}$ (at the centreline) and ν. Its magnitude on the centreline is 0.047. Since the present far-wake satisfies self-preservation to a close approximation (Tang *et al.* 2015*b*), the diffusion term in (2.8) should behave as the advection term in (3.4) (C_a/R_λ) but with a different constant (C_d), *viz.*

$$-\frac{3}{7\nu}\frac{\partial\overline{u_2\epsilon_1}}{\partial x_2}\bigg/\left[\frac{\bar{\epsilon}_{iso}^{3/2}}{(15\nu)^{3/2}}\right] = \frac{C_d}{R_\lambda}, \tag{3.6}$$

where $C_d = 1.9$ (estimated at $R_\lambda = 40$, *viz.* $C_d/R_\lambda = 0.047$).

Thus, (2.8) can finally be rewritten as

$$S + 2\frac{G}{R_\lambda} = \frac{C}{R_\lambda}, \tag{3.7}$$

where $C = C_a + C_d$. While expressions (3.5) and (3.6) show that C is Reynolds number independent, it is possible that its numerical value depends on the cylinder geometry, which affects the large-scale motion (see also Tang *et al.* (2015*a*) who discussed the constancy of C and its dependence on the initial conditions).

Equation (3.7) is a relation between S, G, R_λ and C (constant) on the centreline of the far-wake. The first objective in deriving (3.7) is to assess the way $S + 2G/R_\lambda$

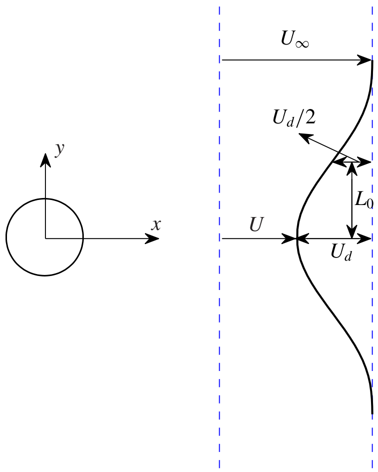

FIGURE 2. (Colour online) Schematic arrangement and coordinate axis.

approaches zero along the centreline of the far-wake as R_λ increases, and to compare this approach with those observed in three other flows: decaying HIT, the axis of a turbulent round jet and SFPBT. As noted in the Introduction, since the ratio G/R_λ approaches a constant relatively rapidly with increasing R_λ, and the term on the right-hand side of (3.7) must eventually vanish, S should become constant at sufficiently large R_λ. This will be addressed in detail in § 5.

4. Experimental details

Experiments have been carried out in a non-return blower-type wind tunnel with a square cross section (350 × 350 mm) of 2.4 m in length. The inclination of the bottom wall of the working section was adjusted in order to maintain a zero streamwise pressure gradient. The wake is generated by a cylinder ($d = 3$, 6 or 12.6 mm), which was installed horizontally in the mid-plane and spanned the full width of the working section (figure 2). It is located 10 cm downstream of the exit plane of the contraction. This resulted in a maximum blockage of approximately 3.6 % and an aspect ratio of 28 when the bigger cylinder ($d = 12.6$ mm) was used. Several values of the Reynolds number $R_d = U_\infty d/\nu$, based on the free-stream velocity U_∞, and the diameter of the cylinder d, are used: 600, 1000, 2000, 3000, 4000, 5880 and 8900. The corresponding Taylor microscale Reynolds number $R_\lambda = u'\lambda/\nu$, based on the Taylor microscale λ and u', the r.m.s. of the streamwise velocity fluctuation, ranged from 23 to 123 in the far-wake. The measurement locations were at $x/d > 170$ for all cases.

The Wollaston (Pt–10 %Rh) hot wires (diameter $d_w = 2.5$ μm) used for the measurements are etched to an active length of approximately $l_w = 0.5$ mm. The length to diameter ratio of the wires is typically 200. In the far-wake, the ratio l_w/η ($\eta = (\nu^3/\overline{\epsilon}_{iso})^{1/4}$ is the Kolmogorov length scale) is smaller than 1 for $R_d = 600$ and 1000 (see figure 3) and smaller than 2 for $R_d = 2000$, 3000, 4000, 5880 and 8900. Figure 3 shows the variations of l_w/η (an indicator of the spatial resolution of the wire) calculated with the measured energy dissipation rate $\overline{\epsilon}_{spec}$ and the energy dissipation rate, $\overline{\epsilon}_{spec}$, estimated from the spectral chart method of Djenidi & Antonia (2012). The ratio l_w/η, when η is calculated using $\overline{\epsilon}_{spec}$, is

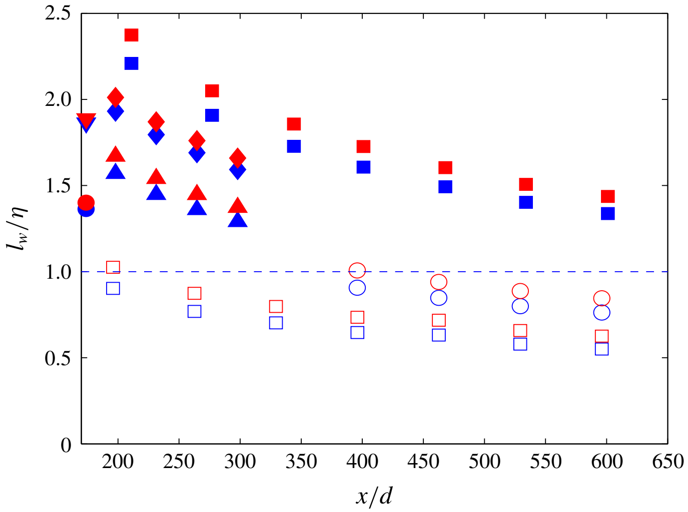

FIGURE 3. (Colour online) Ratio l_w/η. The horizontal line corresponds to $l_w/\eta = 1$. □, $R_d = 600$; ○, 1000; ■, 2000; ▲, 3000; ◆, 4000; ●, 5880; ▼, 8900. Blue and red symbols correspond to $\eta = (\nu^3/\overline{\epsilon}_{iso})^{1/4}$ and $\eta = (\nu^3/\overline{\epsilon}_{spec})^{1/4}$ respectively. Note that for $R_d = 600$, 1000 and 2000, $d = 3$ mm; for $R_d = 3000$ and 4000 $d = 6$ mm; and for $R_d = 5880$ and 8900 $d = 12.6$ mm.

systematically greater than that based on $\overline{\epsilon}_{iso}$, but only by about 10 % at most. The ratio $(l_w/\eta_{iso})/(l_w/\eta_{spec}) = (\eta_{spec}/\eta_{iso}) = (\overline{\epsilon}_{iso}/\overline{\epsilon}_{spec})^{1/4}$, reflects the variation of $(\overline{\epsilon}_{iso}/\overline{\epsilon}_{spec})$ observed in figure 7 below. Browne *et al.* (1987), who measured all components of $\overline{\epsilon}$ in the far wake, also observed a difference of approximately 30 % between $\overline{\epsilon}$ and $\overline{\epsilon}_{iso}$ and showed that only $\overline{\epsilon}$ provided a satisfactory closure of the one-point energy budget. This gives us confidence that the values of $\overline{\epsilon}_{spec}$ must be very close to the actual energy dissipation rates. To determine whether or not the probe resolution can affect the estimate of $\overline{\epsilon}_{iso}$ we show in figure 4 the distributions of $(k_1 l_w)^2\phi_u(k_1 l_w)$ at $R_d = 2000$, which is the worst case scenario in the context of probe resolution. We normalized the spectra by l_w because it is a fixed and accurately known quantity. It can be seen that the contributions to $\overline{\epsilon}_{iso}$ from wavenumbers $k_1 l_w \geqslant 1$ ($k_1 l_w = 1$ corresponds approximately to $k_1\eta = 0.5$ and is the worst case) are small for all x/d, and become smaller as x/d increases. This is confirmed by the ratio $\int_1^\infty (k_1 l_w)^2\phi_u(k_1 l_w)\,\mathrm{d}(k_1 l_w)/\int_0^1 (k_1 l_w)^2\phi_u(k_1 l_w)\,\mathrm{d}(k_1 l_w)$, which quantifies the relative contributions from $k_1 l_w \geqslant 1$ and $k_1 l_w \leqslant 1$ to $\overline{\epsilon}_{iso}$. This ratio decreases from 13 % to 2 % as x/d increases from approximately 200 to 600. For the measurements at smaller R_d, the situation only improves. This provides further confidence in the estimate of $\overline{\epsilon}_{iso}$. In the next section we discuss further the difference between $\overline{\epsilon}_{iso}$ and $\overline{\epsilon}_{spec}$. The hot wires are operated with constant-temperature anemometers at an overheat ratio of 1.5. The output signals from the anemometers were passed through buck and gain circuits and low-pass filtered (the cutoff frequency f_c, which was in the range 800–8000 Hz depending on the transverse position of the probe and R_d). The filter cutoff frequency f_c was set at approximately $1.4f_\eta$ ($f_\eta = U/2\pi\eta$ is the Kolmogorov frequency). This is large enough to prevent any signal attenuation, even at the largest Reynolds number considered here. Further, since the major contribution to $\overline{\epsilon}_{iso}$ (at least 90 %) is provided by $k_1\eta \leqslant 0.5$, it is most unlikely that our estimates of $\overline{\epsilon}_{iso}$

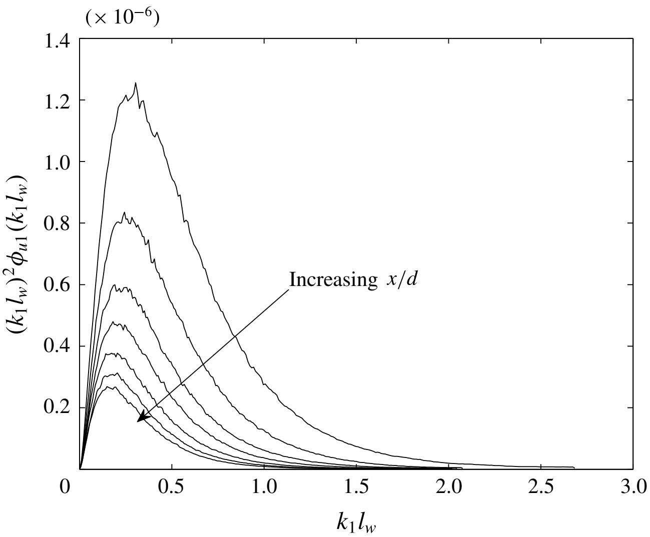

FIGURE 4. Distributions of $(k_1 l_w)^2\phi_u(k_1)$ at $R_d = 2000$.

have been affected by the present cutoff frequency of the filter. The signal is then digitized into a personal computer using a 12 bit analog-to-digital (A–D) converter at a sampling frequency ($\approx 2f_c$) in the range 1600–16 000 Hz. The record duration, which varied between 100 and 140 s, is sufficient for the second- and third-order moments to converge according to the criteria proposed by Anselmet *et al.* (1984) and Camussi & Guj (1995).

5. Results

5.1. *Estimates of R, R_ϵ, and G*

The expression for the advection term, (3.4), contains two ratios: R and R_ϵ. Before testing (3.7), the choices of R and R_ϵ require some discussion. For $R_d = 2000$, Hao *et al.* (2008) showed that both $\overline{u_1^2}/\overline{u_2^2}$ and $\overline{u_1^2}/\overline{u_3^2}$ are approximately 1.4 (i.e. $R = 0.71$) on the centreline in the far-wake of a circular cylinder. Antonia & Browne (1986) and Zhou, Antonia & Tsang (1998, 1999) found that the Reynolds stresses ($\overline{u_1^2}$, $\overline{u_2^2}$, and $\overline{u_1u_2}$) in the far-wake collapsed reasonably well over the range $R_d = 1170$–2800 when plotted after normalizing by the maximum velocity defect and the wake half-width. A value of R close to 0.71 was also obtained by Zhou *et al.* (1998, 1999) at $R_d = 9700$.

Tang *et al.* (2015*b*) showed that the flow in the far-wake satisfies complete self-preservation to a close approximation. This hinges on R_λ remaining constant with respect to x. Figure 5 shows that R_λ is indeed constant along the centreline of the far-wake for any given value of R_d (note that for $R_d = 4000$, a bigger cylinder is used, see figure 2). This is further confirmed by the distributions of $\phi_u^*(k_1^*)$ ($\phi_u^*(k_1^*)$ is the one-dimensional spectral density of u, defined such that $\int_0^\infty \phi_u(k_1)\,\mathrm{d}k_1 = \overline{u^2}$), normalized by $\bar{\epsilon}_{iso}$ and ν, at all R_d as shown in figure 6(*a*). For a fixed R_d, all spectra of u along the x axis in the far-wake collapse almost perfectly (this is not shown here; such a plot can be found in Tang *et al.* (2015*b*)) irrespective of the combination of velocity and length scales used for normalizing ϕ_u, e.g. Kolmogorov velocity scale ($u_K = (\nu\bar{\epsilon}_{iso})^{1/4}$) and η, u' and λ or U_d and L_0. When R_d is varied, the

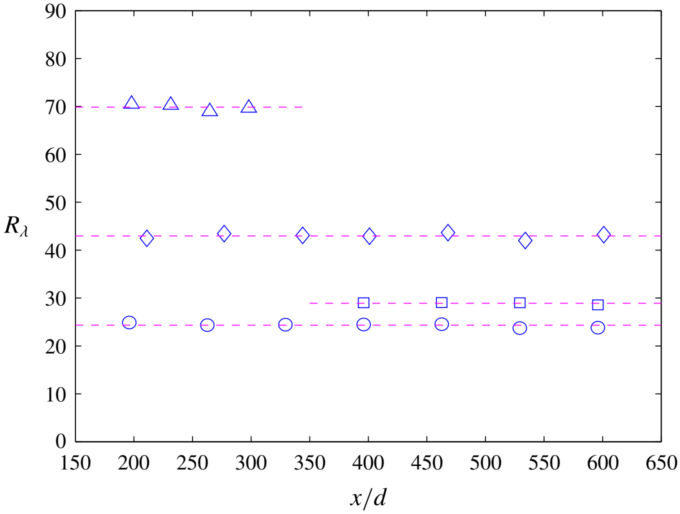

FIGURE 5. (Colour online) Streamwise variation in R_λ on the flow centreline. $R_d = 600$, ○; $R_d = 1000$, □; $R_d = 2000$, ◇; $R_d = 4000$, △. The horizontal dashed lines indicate the mean values of the present data at each R_d.

Kolmogorov-normalized spectra of u in the far-wake region do not collapse over the low wavenumber range (figure 6*a*), which is not surprising. However, the collapse is not perfect in the dissipative range; this is mainly because $\bar{\epsilon}_{iso}$ has been used in figure 6(*a*), the actual $\bar{\epsilon}$ not being known. This imperfect collapse is not easily discernible on the log–log scales of figure 6(*a*). It is however quite evident when $k_1^{*4}\phi_u^*(k_1^*)$ is plotted against k_1^* on a linear scale, as in figure 6(*c*). The distributions in $k_1^{*4}\phi_u^*(k_1^*)$ (figure 6*c*) show an unmistakable systematic decrease as R_d (or R_λ) increases. In an attempt to obtain more accurate values of the energy dissipation rate, the spectral chart method of Djenidi & Antonia (2012) has been applied to the present spectra, when plotted in the form $\phi_u(f)$ versus f. The 'new' estimates of $\bar{\epsilon}$ are denoted by $\bar{\epsilon}_{spec}$. In essence, these values ensure that there is collapse in the upper part of the dissipative range, as illustrated in figure 6(*b*) (the corresponding distributions of $k_1^{*4}\phi_u^*(k_1^*)$ are shown in figure 6*d*). Since this collapse has a solid analytical underpinning (we recall here that the assumption of local isotropy (LI) was relaxed in Antonia, Djenidi & Danaila (2014) to an assumption of local axisymmetry) $\bar{\epsilon}_{spec}$ should be very close to the true value of $\bar{\epsilon}$. Whilst the collapse in figure 6(*b*,*d*) may seem contrived, the values of $\bar{\epsilon}_{spec}$ provided by the spectral method are in fact quite plausible, as will be seen below, and are supported by experimental estimates of $\bar{\epsilon}$ in the far-wake. Estimated values of the ratio $R_\epsilon = \bar{\epsilon}_{iso}/\bar{\epsilon}_{spec}$, where $\bar{\epsilon}_{iso}$ is inferred from measured values of $\overline{(\partial u/\partial x)^2}$ and $\bar{\epsilon}_{spec}$ is estimated via the spectral chart, are shown in figure 7. Antonia & Browne (1986) and Browne *et al.* (1987) measured all components of $\bar{\epsilon}$ at $R_d = 1170$ and were able to close the one-point energy budget, at least indirectly (the pressure term was not measured but was inferred by difference; its integration across the wake yielded a value close to zero). They found that $R_\epsilon = 0.7$, i.e. a significant difference between $\bar{\epsilon}_{iso}$ and $\bar{\epsilon}$. Also included is the analytical estimate of Tang *et al.* (2015*b*) for $R_d = 2000$ and the estimates by Champagne (1978) for $R_\lambda = 138$ and 182, respectively. All these data are in reasonable agreement with each other. R_ϵ is expected to approach the value of one at sufficiently large R_λ,

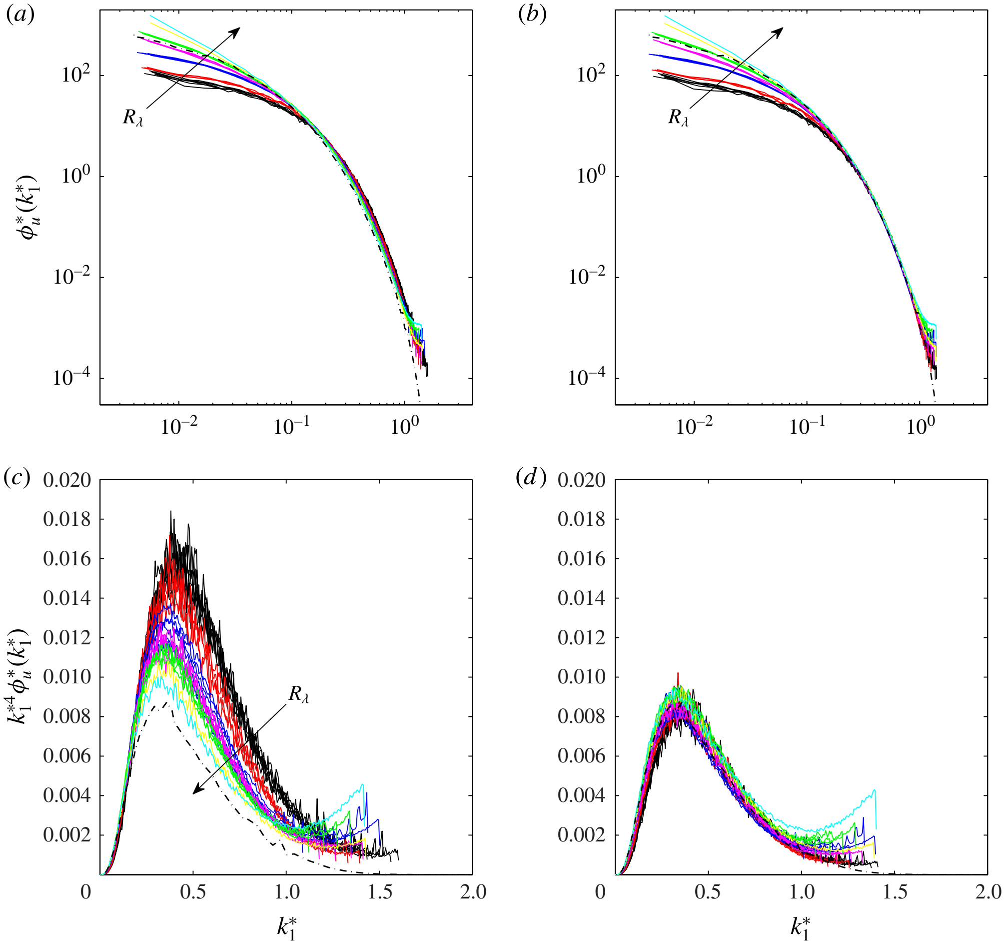

FIGURE 6. (Colour online) Distributions of the Kolmogorov-normalized one-dimensional longitudinal velocity spectrum and the integrand of $2G/R_\lambda$, (5.2). (*a*) Normalization by $\bar{\epsilon}_{iso}$ and ν; (*b*) normalization by $\bar{\epsilon}_{spec}$ and ν. The black dashed curve corresponds to the DNS velocity spectrum on the centreline of a fully developed channel flow (Abe, Antonia & Kawamura 2009). $R_d = 600$, 1000, 2000, 3000, 4000, 5880 and 8900; the arrow indicates the direction R_λ increases. (*c*,*d*) Show $k_1^{*4}\phi_u^*(k_1^*)$, which correspond to the spectra in (*a*,*b*) respectively.

which is consistent with figure 7. For $R_\lambda \geqslant 130$, $R_\epsilon \simeq 1.0$. We recall that (2.1) was obtained along the axis in the far-wake with the assumption of LI. Figure 7 shows that this assumption becomes more tenable as R_λ increases. The departure from LI is approximately 10 % at $R_\lambda \simeq 100$ and LI, at least in the context of $\bar{\epsilon} \simeq \bar{\epsilon}_{iso}$, seems to be satisfied adequately for $R_\lambda \geqslant 130$. When testing (3.7), a polynomial fit to the distribution of R_ϵ is used, i.e. $R_\epsilon = f(R_\lambda)$, which is also shown in figure 7.

To estimate G, a uniform treatment was applied to the measured distributions of $\phi_u^*(k_1^*)$ (figure 6*b*) primarily to avoid the effects of noise contamination and possible inadequate spatial resolution of the hot wire. It can be seen from figure 6(*b*) that, for $k_1^* > 0.7$–1 (depending on R_λ), the spectra are affected by high-frequency noise.

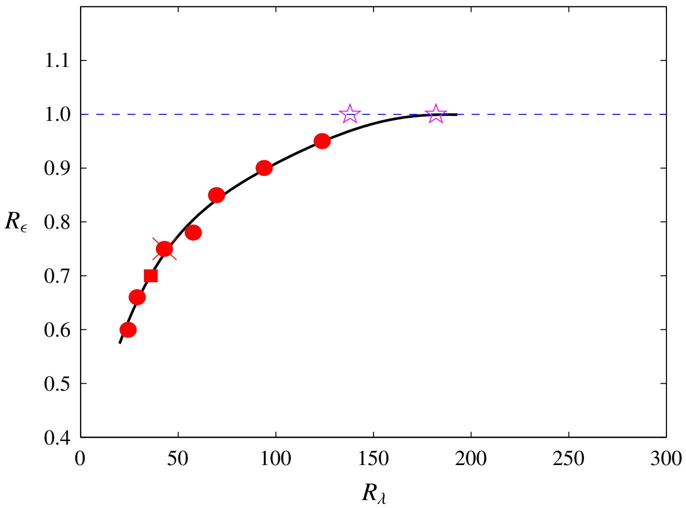

FIGURE 7. (Colour online) Variation of $R_\epsilon = \bar{\epsilon}_{iso}/\bar{\epsilon}_{spec}$ with R_λ. ●, present data; ×, Tang *et al.* (2015*b*); ■, Browne *et al.* (1987); ☆, Champagne (1978). The solid curve is a polynomial fit to all the data.

Nevertheless, all the measured and DNS spectra collapse well in the range of $k_1^* <$ 0.7–1. The measured spectrum beyond $k_1^* \approx 0.7$–1 (the precise value depends on R_λ) was ignored and a suitable fit to the well resolved DNS data (see figure 6*b*,*d*) was applied to the lower end of the dissipation range before extrapolating to a value of k_1^* of 2. The robustness of the collapse of the spectra at sufficiently large k_1^* underpins the extrapolation used here for estimating G. There is now ample experimental, numerical and theoretical evidence that a significant portion of the Kolmogorov normalized spectrum beyond $k_1^* \approx 0.5$ is universal (see for example Antonia *et al.* (2014)) which justifies the extrapolation of the spectrum in the dissipative range (details of the procedure are given in Tang *et al.* (2015*a*), see also Lee *et al.* (2013), and are not repeated here).

The term G, defined by (1.5), can be rewritten as

$$G = \frac{\overline{u_1^{*2}}\,\overline{(\partial^2 u_1^*/\partial x_1^{*2})^2}}{\overline{(\partial u_1^*/\partial x_1^*)^2}^2}, \tag{5.1}$$

where the asterisk denotes normalization by the Kolmogorov scales. If LI holds, so that $\overline{\epsilon} = \overline{\epsilon}_{iso}$, (5.1) can be rewritten as

$$\frac{2G}{R_\lambda} = 2 \times 15^{3/2} \int_0^\infty k_1^{*4} \phi_u^*(k_1^*)\,\mathrm{d}k_1^*. \tag{5.2}$$

However, if there is a departure from LI, then $2G/R_\lambda$ should be estimated using

$$\frac{2G}{R_\lambda} = 2\nu \frac{\displaystyle\int_0^\infty {k_1}^4 \phi_u(k_1)\,\mathrm{d}k_1}{\left[\displaystyle\int_0^\infty {k_1}^2 \phi_u(k_1)\,\mathrm{d}k_1\right]^{3/2}}. \tag{5.3}$$

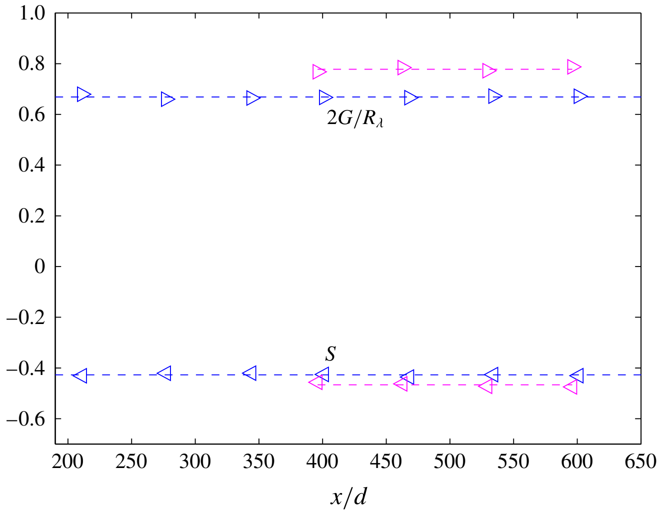

FIGURE 8. (Colour online) Variation of $2G/R_\lambda$ and S with x/d for $R_d = 1000$ (pink) and 2000 (blue). The horizontal dashed line indicates the mean value for each of the plotted quantities.

As seen earlier, there are departures from LI for $R_\lambda \leqslant 130$ along the centreline of the far-wake. Here, we estimate $2G/R_\lambda$ from (5.3) after extrapolation of $\phi_u^*(k_1^*)$ (figure 6*b*) and converting $\phi_u^*(k_1^*)$ to $\phi_u(k_1)$. As an example, two sets of values $2G/R_\lambda$ ($R_d = 1000$ and 2000) are shown in figure 8. Also shown are the corresponding values of S at these two R_d. It is clear that both $2G/R_\lambda$ and S are constant in the far-wake since the flow satisfies complete self-preservation quite closely. Thus, for the present data, each value of $2G/R_\lambda$ and S, (also $S + 2G/R_\lambda$), shown hereafter is an average of values measured at several x locations ($\geqslant 170d$) since they do not vary (see figure 8) with x. For $R_d = 5880$ and 8900, measurements were made at only one location (see figure 3).

5.2. *Boundedness of S*

Estimates of $2G/R_\lambda$ for the present flow are shown in figure 9. Also included in figure 9 are estimates inferred from measured spectra along the axis of a pipe by Rosenberg *et al.* (2013) and the active grid turbulence investigated by Larssen & Devenport (2011). Both sets of measurements were carried out over a relatively large range of R_λ. Antonia *et al.* (2015) and Tang *et al.* (2015*a*) showed that $2G/R_\lambda$ is very nearly constant (≈ 0.52) for $R_\lambda \geqslant 70$ in various flows such as along the axis of a pipe, grid turbulence and along the centreline of the channel, while the constancy of $2G/R_\lambda$ is achieved at smaller R_λ in SFPBT. For the present flow along the centreline of the far-wake, the approach appears to become slower ($R_\lambda \geqslant 100$) than the other flows considered by Antonia *et al.* (2015) and Tang *et al.* (2015*a*), possibly due to the departure from LI along the centreline of the far-wake.

Antonia *et al.* (2015) and Tang *et al.* (2015*a*) showed that $-S$ should approach a universal constant when R_λ is sufficiently large, but the way this constant is approached depends on the flow and, for a given flow, is likely to depend on the initial conditions. For example, the approach is slow in grid turbulence and along the centreline of a channel but rapid along the axis of a round jet. The values of $-S$ for the present flow are shown in figure 10 as a function of R_λ. Also included are the

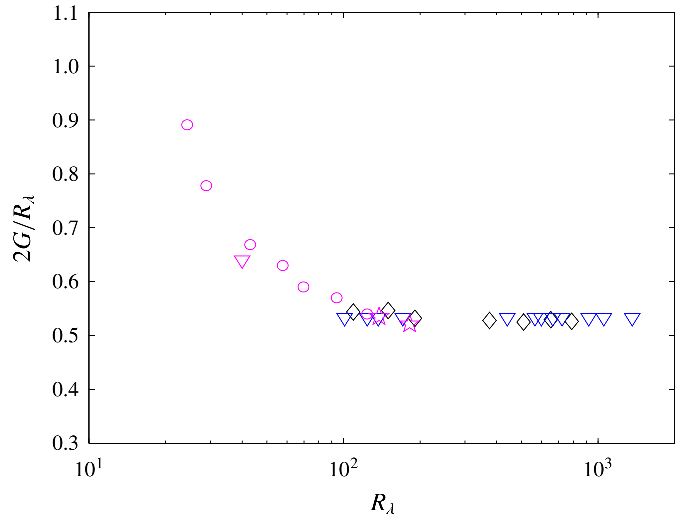

FIGURE 9. (Colour online) Dependence of $2G/R_\lambda$ on R_λ along the centreline of the far-wake: ○, present data; ▽, Lefeuvre *et al.* (2014) ($R_\lambda = 40$); ☆, Champagne (1978). Estimates from Larssen & Devenport (2011) (▽) and Rosenberg *et al.* (2013) (◇) are also shown for the purpose of comparison.

data of Antonia, Zhou & Romano (2002) measured at $x/d = 70$ of a circular cylinder. For reference, the analytical prediction of Qian (1994) (green curve) are shown, whereas the data for other flows, such as grid turbulence, the centreline of a channel and the axis of a round jet are not shown since they have been discussed in detail by Antonia *et al.* (2015) and Tang *et al.* (2015*a*). As noted by Antonia *et al.* (2015) and Tang *et al.* (2015*a*), the magnitude of S should be virtually constant in SFPBT; the value of 0.52 is in good agreement with the analytical prediction of Qian (1994). For the self-preserving cylinder wake data, $-S$ decreases initially as R_λ increases between 20 and 40. For $R_\lambda > 40$, $-S$ starts to increase slowly up to $R_\lambda \simeq 100$ and somewhat more rapidly beyond $R_\lambda = 100$. The main message of figure 10 is that the magnitude of S and its variation with R_λ differs between the two flows. More importantly, the distribution of S, estimated from $S = C/R_\lambda - 2G/R_\lambda$ after assuming $2G/R_\lambda = \text{const.}$ (≈ 0.52 for $R_\lambda > 90$) is reasonably well supported by the present two data points ($R_\lambda = 94$ and 124) as well as the data of Champagne (1978) at $x/d = 299$, and Antonia *et al.* (2002) at $x/d = 70$. Interestingly, the behaviour of S with R_λ is reminiscent of that observed in decaying HIT (Tavoularis, Bennett & Corrsin 1978; Mansour & Wray 1994). It was found as R_λ increases from very low values, $-S$ first increases, reaches a local maximum, decreases and increases again. There is no explanation yet for this behaviour.

Figure 11 shows $S + 2G/R_\lambda$ versus R_λ in different flows. In this figure, the 4 curves (pink solid, black solid, dash-dotted and dotted curves) inferred from (3.7), where C is a flow-dependent constant as noted in the Introduction, correspond to the centreline of a self-preserving cylinder wake, grid turbulence, the axis of a round jet and SFPBT, respectively. Symbols are the experimental data for the present wake. It can be seen from this figure that, along the centreline of the wake, the approach is reasonably well supported by the experimental data. The further following comments can be made on the basis of the results in figures 9–11: (i) due to the fundamental constraint of the

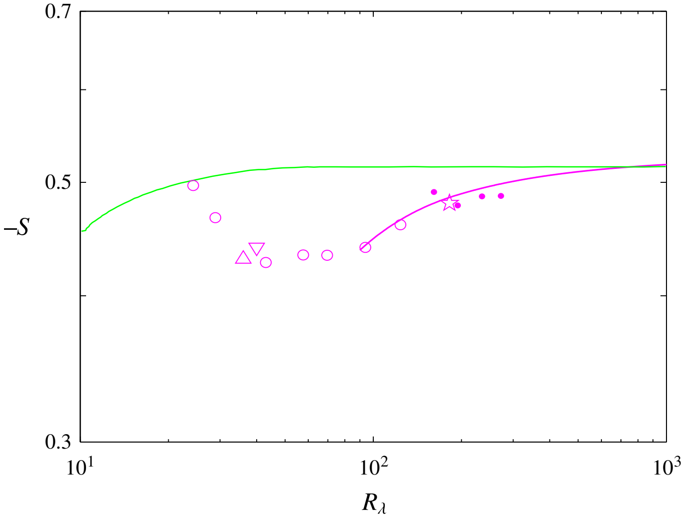

FIGURE 10. (Colour online) Dependence of $-S$ on R_λ along the centreline of the far-wake: ○, present data; △, Browne *et al.* (1987); ▽, Lefeuvre *et al.* (2014); ☆, Champagne (1978). For reference, the prediction of Qian (1994) (green curve) and the data for SFPBT are shown. Also included are the data of Antonia *et al.* (2002) measured at $x/d = 70$ of a circular cylinder (•). The pink curve is inferred from $S = C/R_\lambda - 2G/R_\lambda$ by assuming $2G/R_\lambda = \text{const.}$ (≈ 0.52 for $R_\lambda > 90$) on the centreline of the far-wake.

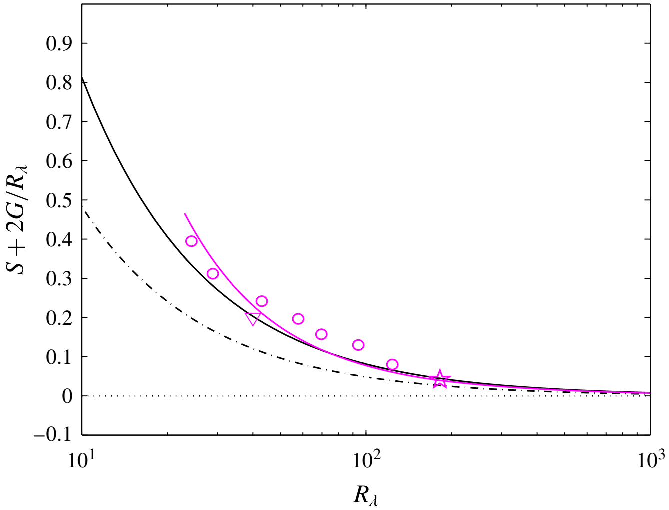

FIGURE 11. (Colour online) Dependence of $S + 2G/R_\lambda$ on R_λ along the centreline of the far-wake: ○; present data; ▽, Lefeuvre *et al.* (2014); ☆, Champagne (1978); four curves (pink solid, black solid, dash-dotted and dotted curves), inferred from (3.7) (C is flow-dependent), correspond to the centreline of the far-wake, grid turbulence, the axis of a round jet and SFPBT, respectively.

mean transport equation for $\overline{\epsilon}_{iso}$ for the flow along the wake centreline, $S + 2G/R_\lambda$ approaches its stationary state ($S + 2G/R_\lambda = 0$) along a path which is different from that in other flows. The approach is slow for the present flow and rapid along the axis of a round jet; (ii) since the term C/R_λ should become negligible at sufficiently large R_λ for the present flow, $-S$ cannot grow unboundedly as R_λ increases since $2G/R_\lambda$ approaches a constant relatively rapidly with increasing R_λ (figure 9). This is consistent with $K41$ and the prediction of Qian (1994). It is also consistent with the predictions of Tennekes (1968) based on a vortex tube model and the heuristic model of Saffman (1970). Further, it does not contravene Ishihara's expectation (Ishihara *et al.* 2007) that 'as $R_\lambda \to \infty$, $-S$ approaches a constant independent of R_λ but the approach may be slow'. We should also finally note that for the forced flow between counter-rotating disks (Tabeling *et al.* 1996; Belin *et al.* 1997), $-S$ is practically constant ($\approx$0.50) over the range $170 \leqslant R_\lambda \leqslant 2000$ notwithstanding a transition at $R_\lambda \approx 700$; these data are not shown in figure 10 as they have been discussed in some detail in Antonia *et al.* (2015). It is not however consistent with $K62$ or the predictions from lognormal and fractal models, (e.g. Frisch, Sulem & Nelkin 1978; Van Atta & Antonia 1980; Frisch 1996; Sreenivasan & Antonia 1997; Davidson 2004; Wyngaard 2010). Strictly, predictions from $K62$, as with $K41$, should be tested at very large R_λ, and under conditions for which LI holds. Unfortunately, this has not been the case since laboratory data, typically obtained in the range $40 < R_\lambda < 1000$, have been used. For these data, the finite Reynolds number effect, which is intimately linked to the dependency of C on the flow, cannot be ignored. Nor can the departure from LI be completely dismissed. High R_λ atmospheric surface layer (ASL) data have also been used in conjunction with laboratory data for testing $K62$. Indeed, these data have been instrumental in the context of providing support for $K62$. As noted in Antonia *et al.* (2015), we cannot however be certain that the ASL data, which were mostly obtained in relatively close proximity to the ground or ocean surface, have not been adversely affected by this proximity.

Finally, it is worthwhile mentioning that the present analysis, which can be applied to other flows, has repercussions for turbulence modelling. For example, Thiesset *et al.* (2014), who applied the analysis to the axis of a turbulent round jet, discussed how new insights can be gained, and in particular, how some turbulence models can be improved. For example, they showed how $(S + 2G/R_\lambda = C/R_\lambda)$ can be used to determine the important model constant $C_{\epsilon 2}$ used in the k–ϵ model; they showed that $C_{\epsilon 2} = 7/8$ on the axis of the turbulent round jet and $(n+1)/n$ in decaying grid turbulence. We can repeat the same analysis of Thiesset *et al.* (2014) to obtain an expression for $C_{\epsilon 2}$. We can write (2.8) as

$$-U\frac{\partial \overline{\epsilon}_{iso}}{\partial x} - \frac{3}{7\nu}\frac{\partial \overline{u_2 \epsilon_1}}{\partial x_2} = C_{\epsilon 2}\frac{\epsilon_{iso}^2}{k}\frac{1}{R_\epsilon^2}, \tag{5.4}$$

which, after trivial manipulation, leads to

$$C_{\epsilon 2} = \tfrac{7}{90}R_\epsilon^2(1+2R)(SR_\lambda + 2G). \tag{5.5}$$

Combining (3.4), (3.6) and (3.7) into the above expression yields

$$C_{\epsilon 2} = R_\epsilon + \tfrac{7}{90}C_d R_\epsilon^2(1+2R). \tag{5.6}$$

If one assumes, $R_\epsilon = 1$ (as expected at large R_λ) and $R = 0.71$ (as measured by Hao *et al.* (2008)), one then obtains $C_{\epsilon 2} = 1.36$ along the centreline of the far-wake. As anticipated, this value differs from both those obtained in decaying grid turbulence and along the axis of a turbulent round jet.

6. Conclusions and concluding discussion

The transport equation for the isotropic turbulent energy dissipation rate $\overline{\epsilon}_{iso}$ along the centreline in the far-wake of a circular cylinder is derived by applying the limit at small separation to the two-point energy budget equation. It is found that the imbalance between the production and the destruction of $\overline{\epsilon}_{iso}$, respectively due to vortex stretching and viscosity, is governed by both the streamwise advection and the lateral turbulent diffusion (the former contributes more to the budget than the latter). This imbalance is intrinsically different from that in other flows, e.g. grid turbulence, and along the centreline of a fully developed channel flow, where either the streamwise advection or the lateral turbulent diffusion of $\overline{\epsilon}_{iso}$ governs the imbalance. It is also different from that in SFPBT where, by definition, the production of $\overline{\epsilon}_{iso}$ is equal to the destruction of $\overline{\epsilon}_{iso}$.

As pointed out by Antonia *et al.* (2015) and Tang *et al.* (2015*a*), the different types of imbalance represent different constraints on the relation between the skewness of the longitudinal velocity derivative S and the enstrophy destruction coefficient G in different flows, i.e. $S+2G/R_\lambda$ approaches the asymptotic state differently in different flows even though $S+2G/R_\lambda \propto R_\lambda^{-1}$ in each case. For example, the approach to zero is slow for the present flow and rapid along the axis of a round jet. This difference reflects, in essence, the different physical processes involved at large scales in the energy budget for these two cases. Along the axis of an axisymmetric jet, $\overline{\epsilon}$ is balanced by the advection of $\overline{q^2}$ along x and a small contribution from production terms associated with the normal Reynolds stresses. On the centreline of the far-wake, $\overline{\epsilon}$ is balanced by the advection of $\overline{q^2}$ along x and an almost equal contribution from the diffusion of $\overline{q^2}$ due to v (i.e. the ratio of the advection term to diffusion term is approximately one). The same physical processes remain at play in the (small scale) budget of $\overline{\epsilon}_{iso}$ while the advection term contributes more to the budget than the diffusion term. Since figure 9 indicates that $2G/R_\lambda$ becomes constant at relatively small R_λ, the combination of figures 9 and 11 suggests that S should become constant in the far-wake at a sufficiently large R_λ, which is strongly supported by figure 10. It should be noted that, for any given flow, there is evidence that S may also depend on initial conditions as reflected for example by the difference in S between different simulations or between simulations and experiments along the centreline of a fully developed channel flow (Tang *et al.* 2015*a*).

It is clear that figures 9–11 have major implications in the context of testing predictions ensuing from $K41$ and $K62$. All previous investigations have included laboratory data for S obtained in a number of flows over the same range of R_λ as in figure 10 without recognising the different types of large scale inhomogeneity that are present in different flows. This is tantamount to ignoring the different finite Reynolds number effects that exist in the different flows. Consequently, previous work which advocates a unique power-law dependence $|S| \sim R_\lambda^\alpha$ $(\alpha > 0)$ must be shrouded with ambiguity and hence treated with caution. However, since complete self-preservation is satisfied, to quite a close approximation, in the far-wake, S, $2G/R_\lambda$, and R_λ do not vary with x, thus removing any ambiguity when plotting $S+2G/R_\lambda$ versus R_λ in the far-wake. The main message conveyed by figures 9–11 is that S is most likely to be bounded in the far-wake, provided the effect of the Reynolds number is negligible. This result is in conflict with $K62$ but is in agreement with $K41$. It is important to stress that $K62$ is based solely on phenomenological arguments which, in view of the present results, seems to conflict with the self-preservation constraints imposed on the Navier–Stokes equations. Clearly, further work will be needed both to confirm the present result and assess if the R_λ dependence of higher order moments of $\partial u/\partial x$, e.g. the flatness factor ($F = \overline{(\partial u/\partial x)^4}/\overline{(\partial u/\partial x)^2}^2$) are, like S, also bounded at sufficiently large R_λ, once the appropriate constraint derived from the N–S equations is established. Such a possibility was anticipated by Qian (1986).

Acknowledgement

The financial support by the Australian Research Council is acknowledged.

REFERENCES

ABE, H., ANTONIA, R. A. & KAWAMURA, H. 2009 Correlation between small-scale velocity and scalar fluctuations in a turbulent channel flow. *J. Fluid Mech.* **627**, 1–32.

ANSELMET, F., GAGNE, Y., HOPFINGER, E. J. & ANTONIA, R. A. 1984 Higher-order velocity structure functions in turbulent shear flows. *J. Fluid Mech.* **140**, 63–89.

ANTONIA, R. A. & BROWNE, L. W. 1986 Anisotropy of temperature dissipation in a turbulent wake. *J. Fluid Mech.* **163**, 393–403.

ANTONIA, R. A., BROWNE, L. W. B., BISSET, D. K. & FULACHIER, L. 1987 A description of the organized motion in the turbulent far wake of a cylinder at low Reynolds number. *J. Fluid Mech.* **184**, 423–444.

ANTONIA, R. A., BROWNE, L. W. B. & SHAH, D. A. 1988 Characteristics of vorticity fluctuations in a turbulent wake. *J. Fluid Mech.* **189**, 349–365.

ANTONIA, R. A. & BURATTINI, P. 2006 Approach to the 4/5 law in homogeneous isotropic turbulence. *J. Fluid Mech.* **550**, 175–184.

ANTONIA, R. A., DJENIDI, L. & DANAILA, L. 2014 Collapse of the turbulent dissipation range on Kolmogorov scales. *Phys. Fluids* **26**, 045105.

ANTONIA, R. A., TANG, S. L., DJENIDI, L. & DANAILA, L. 2015 Boundedness of the velocity derivative skewness in various turbulent flows. *J. Fluid Mech.* **781**, 727–744.

ANTONIA, R. A., ZHOU, T., DANAILA, L. & ANSELMET, F. 2000 Streamwise inhomogeneity of decaying grid turbulence. *Phys. Fluids* **12**, 3086–3089.

ANTONIA, R. A., ZHOU, T. & ROMANO, G. P. 2002 Small-scale turbulence characteristics of two-dimensional bluff body wakes. *J. Fluid Mech.* **459**, 67–92.

BATCHELOR, G. K. & TOWNSEND, A. A. 1947 Decay of vorticity in isotropic turbulence. *Proc. R. Soc. Lond.* A **190**, 534–550.

BELIN, F., MAURER, J., TABELING, P. & WILLAIME, H. 1997 Velocity gradient distributions in fully developed turbulence: experimental study. *Phys. Fluids* **9**, 3843–3850.

BISSET, D. K., ANTONIA, R. A. & BRITZ, D. 1990*a* Structure of large-scale vorticity in a turbulent far wake. *J. Fluid Mech.* **218**, 463–482.

BISSET, D. K., ANTONIA, R. A. & BROWNE, L. W. B. 1990*b* Spatial organization of large structures in the turbulent far wake of a cylinder. *J. Fluid Mech.* **218**, 439–461.

BROWN, G. L. & ROSHKO, A. 2012 Turbulent shear layers and wakes. *J. Turbul.* **13**, 1–32.

BROWNE, L. W., ANTONIA, R. A. & SHAH, D. A. 1987 Turbulent energy dissipation in a wake. *J. Fluid Mech.* **179**, 307–326.

BURATTINI, P., ANTONIA, R. A. & DANAILA, L. 2005 Similarity in the far field of a turbulent round jet. *Phys. Fluids* **17**, 025101.

CAMUSSI, R. & GUJ, G. 1995 Experimental analysis of scaling laws in low and moderate *Re* grid generated turbulence. *Exp. Fluids* **24**, 63–67.

CHAMPAGNE, F. H. 1978 The fine-scale structure of the turbulent velocity field. *J. Fluid Mech.* **86**, 67–108.

DANAILA, L., ANSELMET, F., ZHOU, T. & ANTONIA, R. A. 1999 A generalization of Yaglom's equation which accounts for the large-scale forcing in heated decaying turbulence. *J. Fluid Mech.* **391**, 359–372.

DANAILA, L., ANSELMET, F., ZHOU, T. & ANTONIA, R. A. 2001 Turbulent energy scale-budget equations in a fully developed channel flow. *J. Fluid Mech.* **430**, 87–109.

DANAILA, L., ANTONIA, R. A. & BURATTINI, P. 2004 Progress in studying small-scale turbulence using 'exact' two-point equations. *New J. Phys.* **6**, 2–23.

DAVIDSON, P. A. 2004 *Turbulence: An Introduction for Scientists and Engineers*. Oxford University Press.

DJENIDI, L. & ANTONIA, R. A. 2012 A spectral chart method for estimating the mean turbulent kinetic energy dissipation rate. *Exp. Fluids* **53**, 1005–1013.

DJENIDI, L. & ANTONIA, R. A. 2014 Transport equation for the mean turbulent energy dissipation rate in low-R_λ grid turbulence. *J. Fluid Mech.* **747**, 288–315.

FRISCH, U. 1996 *Turbulence: The Legacy of A. N. Kolmogorov*. Cambridge University Press.

FRISCH, U., SULEM, P. L. & NELKIN, M. 1978 A simple dynamical model of intermittent fully developed turbulence. *J. Fluid Mech.* **87**, 719–736.

FUKAYAMA, D., OYAMADA, T., NAKANO, T., GOTOH, T. & YAMAMOTO, K. 2000 Longitudinal structure functions in decaying and forced turbulence. *J. Phys. Soc. Japan* **69**, 701–715.

GOTOH, T., FUKAYAMA, D. & NAKANO, T. 2002 Velocity field statistics in homogeneous steady turbulence obtained using a high-resolution direct numerical simulation. *Phys. Fluids* **14**, 1065–1081.

HAO, Z., ZHOU, T., CHUA, L. P. & YU, S. C. M. 2008 Approximations to energy and temperature dissipation rates in the far field of a cylinder wake. *Exp. Therm. Fluid Sci.* **32**, 791–799.

HINZE, J. O. 1975 *Turbulence*. McGraw-Hill.

ISHIHARA, T., KANEDA, Y., YOKOKAWA, M., ITAKURA, K. & UNO, A. 2007 Small-scale statistics in high-resolution direct numerical simulation of turbulence: Reynolds number dependence of one-point velocity gradient statistics. *J. Fluid Mech.* **592**, 335–366.

KOLMOGOROV, A. 1941*a* Dissipation of energy in the locally isotropic turbulence. *Dokl. Akad. Nauk SSSR* **32**, 19–21 (see also 1991 *Proc. R. Soc. Lond.* A **434**, 15–17).

KOLMOGOROV, A. N. 1941*b* Local structure of turbulence in an incompressible fluid for very large Reynolds numbers. *Dokl. Akad. Nauk SSSR* **30**, 299–303 (see also 1991 *Proc. R. Soc. Lond.* A **434**, 9–13).

KOLMOGOROV, A. N. 1962 A refinement of previous hypotheses concerning the local structure of turbulence in a viscous incompressible fluid at high Reynolds number. *J. Fluid Mech.* **13**, 82–85.

LARSSEN, J. V. & DEVENPORT, W. J. 2011 On the generation of large-scale homogeneous turbulence. *Exp. Fluids* **50**, 1207–1223.

LEE, S. K., DJENIDI, L., ANTONIA, R. A. & DANAILA, L. 2013 On the destruction coefficients for slightly heated decaying grid turbulence. *Intl J. Heat Fluid Flow* **43**, 129–136.

LEFEUVRE, N., DJENIDI, L., ANTONIA, R. A. & ZHOU, T. 2014 Turbulent kinetic energy and temperature variance budgets in the far-wake generated by a circular cylinder. In *19th Australasian Fluid Mechanics Conference, Melbourne, Paper 106.*

MANSOUR, N. N. & WRAY, A. A. 1994 Decay of isotropic turbulence at low Reynolds number. *Phys. Fluids* **6**, 808–814.

QIAN, J. 1986 A closure theory of intermittency of turbulence. *Phys. Fluids* **29**, 2165.

QIAN, J. 1994 Skewness factor of turbulent velocity derivative. *Acta Mechanica Sin.* **10**, 12–15.

ROSENBERG, B. J., HULTMARK, M., VALLIKIVI, M., BAILEY, S. C. C. & SMITS, A. J. 2013 Turbulence spectra in smooth- and rough-wall pipe flow at extreme Reynolds numbers. *J. Fluid Mech.* **731**, 46–63.

SAFFMAN, P. G. 1970 Dependence on Reynolds number of high-order moments of velocity derivatives in isotropic turbulence. *Phys. Fluids* **13**, 2193–2194.

SREENIVASAN, K. & ANTONIA, R. A. 1997 The phenomenology of small-scale turbulence. *Annu. Rev. Fluid Mech.* **29**, 435–472.

TABELING, P., ZOCCHI, G., BELIN, F., MAURER, J. & WILLAIME, H. 1996 Probability density functions, skewness, and flatness in large Reynolds number turbulence. *Phys. Rev.* E **53**, 1613–1621.

TANG, S. L., ANTONIA, R. A., DJENIDI, L., ABE, H., ZHOU, T., DANAILA, L. & ZHOU, Y. 2015*a* Transport equation for the mean turbulent energy dissipation rate on the centreline of a fully developed channel flow. *J. Fluid Mech.* **777**, 151–177.

TANG, S. L., ANTONIA, R. A., DJENIDI, L. & ZHOU, Y. 2015*b* Consequence of self-preservation in a turbulent far-wake. In *The 9th Symposium on Turbulence and Shear Flow Phenomena (TSFP-9), June 30th–July 3rd, Melbourne, Australia, Paper 300*.

TAVOULARIS, S., BENNETT, J. C. & CORRSIN, S. 1978 Velocity-derivative skewness in small Reynolds number, nearly isotropic turbulence. *J. Fluid Mech.* **88**, 63–69.

TENNEKES, H. 1968 Simple model for the small-scale structure of turbulence. *Phys. Fluids* **11**, 669–671.

THIESSET, F., ANTONIA, R. A. & DANAILA, L. 2013 Scale-by-scale turbulent energy budget in the intermediate wake of two-dimensional generators. *Phys. Fluids* **25**, 115105.

THIESSET, F., ANTONIA, R. A. & DJENIDI, L. 2014 Consequences of self-preservation on the axis of a turbulent round jet. *J. Fluid Mech.* **748**, R2.

VAN ATTA, C. W. & ANTONIA, R. A. 1980 Reynolds number dependence of skewness and flatness factors of turbulent velocity derivatives. *Phys. Fluids* **23**, 252–257.

WYNGAARD, J. C. 2010 *Turbulence in the Atmosphere*. Cambridge University Press.

ZHOU, Y., ANTONIA, R. A. & TSANG, W. K. 1998 The effect of Reynolds number on a turbulent far-wake. *Exp. Fluids* **25**, 118–125.

ZHOU, Y., ANTONIA, R. A. & TSANG, W. K. 1999 The effect of the Reynolds number on the Reynolds stresses and vorticity in a turbulent far-wake. *Exp. Therm. Fluid Sci.* **18**, 291–298.